ARMY RESEARCH LABORATORY

ARL

Uniaxial Tensile Strength and Flaw Characterization of SiC-N

by Jared C. Wright and Jeffrey J. Swab

ARL-TR-6794   **January 2014**

NOTICES

Disclaimers

The findings in this report are not to be construed as an official Department of the Army position unless so designated by other authorized documents.

Citation of manufacturer's or trade names does not constitute an official endorsement or approval of the use thereof.

Destroy this report when it is no longer needed. Do not return it to the originator.

Army Research Laboratory

Aberdeen Proving Ground, MD 21005-5069

Uniaxial Tensile Strength and
Flaw Characterization of SiC-N

Jared C. Wright and Jeffrey J. Swab
Weapons and Materials Research Directorate, ARL

REPORT DOCUMENTATION PAGE		*Form Approved* *OMB No. 0704-0188*

1. REPORT DATE *(DD-MM-YYYY)*	2. REPORT TYPE	3. DATES COVERED (From - To)
January 2014	Final	October 2010–September 2011

4. TITLE AND SUBTITLE	5a. CONTRACT NUMBER
Uniaxial Tensile Strength and Flaw Characterization of SiC-N	W911QX-09-C-0057
	5b. GRANT NUMBER
	5c. PROGRAM ELEMENT NUMBER

6. AUTHOR(S)	5d. PROJECT NUMBER
Jared C. Wright and Jeffrey L. Swab	
	5e. TASK NUMBER
	5f. WORK UNIT NUMBER

7. PERFORMING ORGANIZATION NAME(S) AND ADDRESS(ES)	8. PERFORMING ORGANIZATION REPORT NUMBER
U.S. Army Research Laboratory ATTN: RDRL-WMM-E Aberdeen Proving Ground, MD 21005-5069	ARL-TR-6794

9. SPONSORING/MONITORING AGENCY NAME(S) AND ADDRESS(ES)	10. SPONSOR/MONITOR'S ACRONYM(S)
	11. SPONSOR/MONITOR'S REPORT NUMBER(S)

12. DISTRIBUTION/AVAILABILITY STATEMENT

Approved for public release; distribution is unlimited.

13. SUPPLEMENTARY NOTES

14. ABSTRACT

Large blocks (10.8 × 29.4 × 39 cm³) of SiC-N composition were manufactured by BAE Systems (now CoorsTek Vista Operations) using their proprietary pressure-aided densification process. Quasi-static tensile strength was determined using cylindrical uniaxial tension specimens oriented either parallel or perpendicular to the densification direction. Fractography, using a combination of optical and scanning electron microscopy, identified three critical flaw populations: machining damage, agglomerates, and inclusions. The material exhibited a low Weibull modulus and characteristic strength compared to historical data. Two tensile specimen sizes were employed for strength-size scaling analysis yielding strength data as a function of effective volume. Strength-size scaling analysis, though performed, was hampered by the low Weibull modulus and the presence of multiple flaw populations.

15. SUBJECT TERMS

silicon carbide, uniaxial tension, fractography

16. SECURITY CLASSIFICATION OF:			17. LIMITATION OF ABSTRACT	18. NUMBER OF PAGES	19a. NAME OF RESPONSIBLE PERSON Jared C. Wright
a. REPORT	b. ABSTRACT	c. THIS PAGE			19b. TELEPHONE NUMBER *(Include area code)*
Unclassified	Unclassified	Unclassified	UU	48	410-306-0917

Contents

List of Figures

List of Tables

INTENTIONALLY LEFT BLANK.

1. Introduction

SiC-N is a common ceramic armor material used in the protection of military ground vehicles (*1*). Ceramic vehicle armor is usually comprised of an array of square or hexagonal tiles built into a composite armor package. These packages are composed of a series of encapsulated ceramic inserts mounted on a backing material (*2*). The size and thickness of the embedded ceramic tiles depend upon the specific armor application, but scientific study has been largely limited to tiles less than 40 mm thick, especially versus small caliber threats (*1, 3, 4*). Research and production of ceramic tiles for the protection of both vehicles and personnel is being actively pursued by several companies in the United States and around the world (*5*).

While a substantial amount of research has been accumulated in the manufacture of ceramic armor tiles, less literature is available on the production of very large ceramic components. One issue that may occur in the production of large ceramic components is uneven powder packing during the compaction of the ceramic green body due to interparticle friction and interactions with the pressing die (*6*). This could lead to an increase in flaws such as microcracks or porosity when compared to smaller specimens. Cho et al. studied the tensile strength of SiC-N and SiC-B, with the SiC-B specimens machined from both thin (2.54 cm) and thick (17.27 cm) billets. It was found that the specimens from the thicker billet had a lower tensile strength than the specimens machined from the 2.54-cm billet (*7*).

Ceramics are brittle, and under an appropriate applied tensile load will fracture due to the presence of the largest strength limiting flaw. Weibull theory, based upon a "weakest link" failure theory wherein a brittle material will fail from the most severe flaw in the material, is commonly used to model brittle material strength. Weibull theory describes the strength of a material in terms of characteristic strength (σ_θ) and a Weibull modulus (m). The Weibull modulus reflects the repeatability of test results, while the characteristic strength is defined as the strength at a failure probability of 63.2% (*8*).

The identification and characterization of the critical strength limiting flaw in a material is accomplished through fractography. Fractography uses both optical and scanning electron microscopy (SEM) to analyze the fracture surface of a specimen to determine the strength limiting flaw from which fracture originated. Characterization of a specimen's critical flaw is important because flaws originate from different stages during the production process. Flaws associated with the processing of the material (pores, agglomerates, inclusions, large grains, local compositional variations, etc.) can occur throughout the material and each will have their own distribution of size and occurrence (*9*). Each of these flaws might be caused by a different processing variable, and thus could be controlled by different corrective actions. Also, each critical flaw type causes the material to have a distinct Weibull distribution and characteristic strength. These distributions may overlap with each other if the flaws are of similar size or

geometry. Proper classification of strength-limiting flaws can then be used to refine the manufacturing process (*10–12*). Flaws associated with the manufacture of the specimen itself are also important to characterize. Ceramics in particular are susceptible to grinding damage associated with specimen preparation. Machining flaws originating from the manufacture of a test specimen may not represent the flaws that may cause fracture of an actual component in service. Fractography is an essential tool for the evaluation of ceramic strength specimens as it allows for an understanding of the cause of fracture (*13*).

Fracture mechanics can be used to aid fractography by predicting the critical flaw size (c) as a function of flaw shape (Y), measured strength (σ_f), and material fracture toughness (K_{Ic}) as seen in equation 1. This relationship of strength being a function of the flaw size and fracture toughness was first presented by Griffith (*14*). The flaw size (c) is the measured flaw depth in the case of surface flaws, or the flaw radius in the case of volume located flaws. In equation 1, the geometrical term (Y) summarizes flaw location, geometry, and loading conditions; typically having a value between 1 and 2 (*13*). Many things may cause deviations from this model including variations in local fracture toughness or flaw sharpness, local internal stress, or interactions with other nearby flaws. Because of these variations, the size of a calculated flaw and an observed fracture origin can differ by as much as a factor of 2 (*13, 15*). Equation 1 shows the fracture mechanics model used with fractography to predict flaw size.

$$c_{calc} = \left(\frac{K_{Ic}}{Y\sigma_f}\right)^2 \tag{1}$$

In addition to the variables described in equation 1, the test methodology used to determine the critical stress (σ_f) can also influence the measured strength of a material. The dependence of strength on flaw size, location, orientation, and test methodology makes the question of "strength" very difficult, especially for design purposes (*10, 11, 16*). Because it is often either difficult or prohibitively expensive to test a large number of actual ceramic components, it is common practice to machine test specimens from the component and use those test results to estimate the strength of the actual component. The test specimen size, geometry, and method by which a specimen is tested can greatly affect the measured strength value. The most common testing methodology for tensile strength of ceramic material is the American Society for Testing and Materials (ASTM) C1161, which provides a standard template for completing flexure experiments in either three-point or four-point bending (*17*). A schematic of three- and four-point bending is shown in figure 1, with a typical specimen size of $3 \times 4 \times 50$ mm^3. The strength measured by these two tests can be different even when using identically prepared specimens. The reason for this difference in strength can be seen in figure 1 in red at the location of the maximum tensile strength. In a bend (flexure) test, there exists a large stress gradient within the material (fully half of the specimen is placed under compressive loading), with only a small portion at the bottom surface of each specimen actually experiencing the maximum tensile stress.

As flaws in ceramic materials preferentially lead to fracture under a tensile load, flaws located on the tensile surface of a flexure specimen are much more likely to initiate fracture than a flaw located elsewhere in the specimen. Mathematically the region of the sample experiencing the maximum tensile stress can be expressed in terms of either effective surface area (S_E) or effective volume (V_E). Often it is assumed that the flaws within a ceramic material are uniformly distributed; thereby, requiring a large sample population to allow for all flaw types to stochastically appear within the region of maximum tensile stress. From figure 1, the chance of a severe flaw being located in the region of maximum tensile stress in a three-point bend test is significantly less than that of a four-point bend test because of the smaller region of maximum tension. This decrease in effectively tested specimen volume leads to an increase in observed three-point bend strength on the order of 15% over that of four-point bend specimens of the same material (*18*). Data from one test configuration may be compared to other configurations using strength-size scaling (*8, 16, 18–20*).
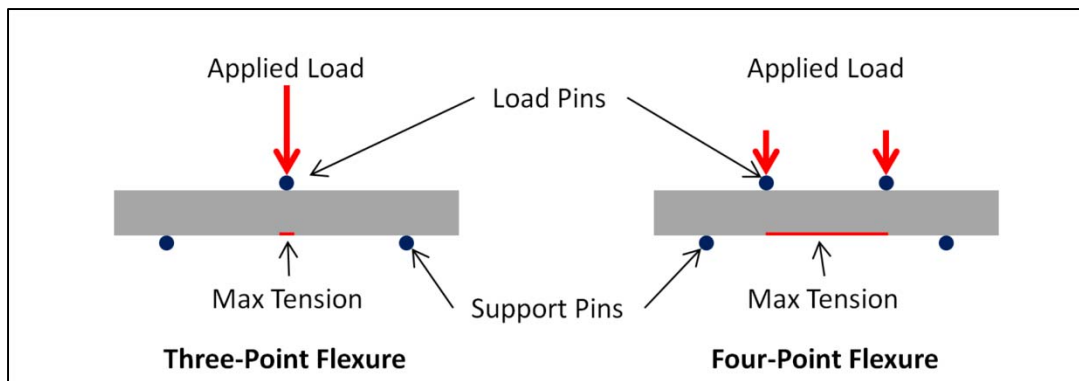
Figure 1. Comparison of flexure methods showing a comparison of the area of each specimen placed in maximum tension.

Strength-size scaling is best accomplished by testing a variety of specimen sizes. The trend established by these results can then be used to scale up to the size of the actual component for a more accurate prediction of component strength. The vast majority of strength data for ceramic materials has been obtained using three-point or four-point flexure techniques. SiC-N has been reported by Ray et al. to have a Weibull characteristic strength of 597 MPa and a Weibull modulus of 8.5 (*21*). Ray et al. measured strength according to ASTM C1161 using "B" sized specimens ($3 \times 4 \times 50$ mm^3). Wereszczak et al. did a complete strength-size scaling analysis of SiC-N focusing on surface related flaws associated with two different surface finishes—but used an equibiaxial flexure methodology described in ASTM C1499 (*22, 23*). A study by Cho et al. measured the uniaxial tensile strength of SiC-N. Specimens were straight right cylinders with a gauge section 8.8-mm in diameter and 40-mm long ($V_E = 2432$ mm^3, $S_E = 1105$ mm^2) (*7*). Two groups of specimens were machined by two different machinists. Characteristic strength and Weibull modulus were reported to be $\sigma_\theta = 359$ MPa and $m = 10.9$ for the first and $\sigma_\theta = 318$ MPa and $m = 15.7$ for the second. The majority of these specimens fractured from flaws located at the specimen surface.

The major disadvantage of flexure testing is that specimens typically fracture from surface or near surface located flaws due to the stress gradient in the test specimen. It is possible for flaws randomly distributed throughout the bulk material to appear on the tensile surface; however, experience indicates that for SiC-N the vast majority of flexure specimens fail from machining damage (*22*). In order to adequately characterize volume-distributed flaws in SiC-N a different test methodology is required. ASTM C1273 is a standard test method to determine the uniaxial tensile strength of ceramics, but the recommended specimens are larger, more difficult to machine, and significantly more expensive than the typical flexure specimen (*24*). Consequently, uniaxial tensile strength data for most ceramics is limited. The advantage of conducting uniaxial tension tests is the increased likelihood that fracture will initiate from volume distributed flaws since a large volume of material is subjected to a uniform maximum tensile stress compared to a flexure specimen. Fractography of these specimens could reveal processing flaws that lead to fracture in situations where surface condition is not a factor. The data generated from uniaxial tension experiments can also be useful in simulation efforts where fracture is anticipated to initiate within the bulk of a material.

In the present report, the uniaxial tensile strength of SiC-N is obtained using cylindrical buttonhead specimens with two different effective volumes. Fractography is used to characterize the critical flaw populations and Weibull statistics applied to examine strength-size scaling. Another cylindrical uniaxial tension specimen, with an effective volume smaller than either of the specimens used in this effort, is presented for possible future strength-size scaling work.

2. Experimental Procedure

Tensile specimens were machined from two large blocks of SiC-N fabricated by BAE Systems (now CoorsTek Vista) via Pressure Aided Densification (PAD), a form of hot pressing. The blocks were nominally $10.8 \times 29.4 \times 39$ cm^3 in size, an example of which can be seen in figure 2. In this report, the blocks are labeled B1 and B2, respectively.

Figure 2. SiC-N monolith used to manufacture tensile specimens.

Two types of tensile specimens were obtained from the SiC-N monoliths. The first configuration was 160 mm long, with a nominal gauge-section diameter of 6.33 mm and length of 35 mm, following the recommendations of ASTM Standard Test Method C1273. The second configuration was similar in design to the first, but was 100 mm long with a gauge section nominally 5.5 mm in diameter and 20 mm long. The two specimen dimensions provide gauge section areas of 696 mm^2 and 346 mm^2 and effective volumes of 1100 mm^3 and 475 mm^3, respectively. The specimen dimensions were chosen to enable strength-size scaling analysis. Figure 3 shows the two specimen geometries tested.
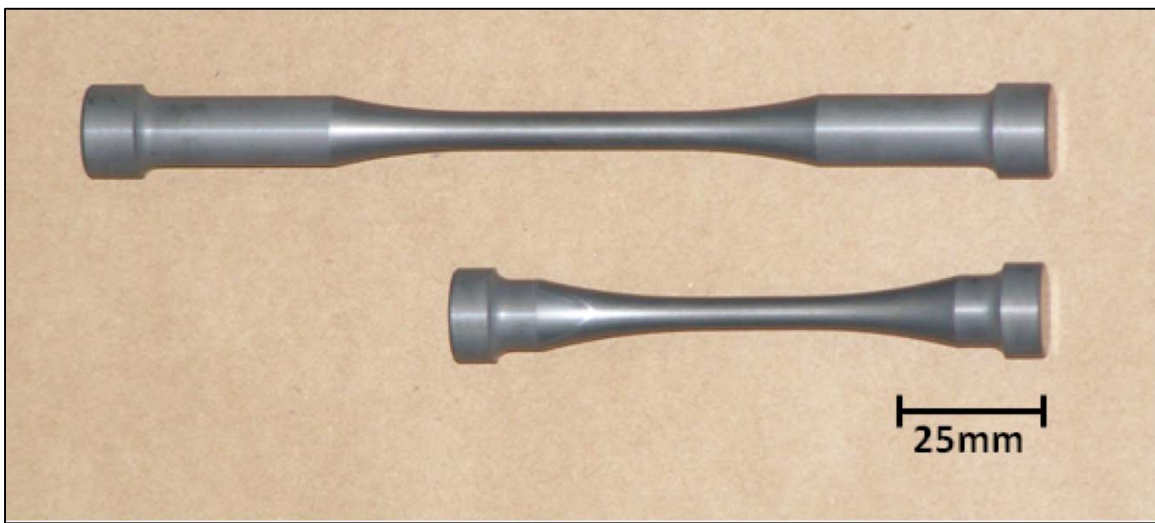
Figure 3. SiC-N uniaxial tension specimen configurations.

The long axes of both specimens were cut from material aligned in the plane perpendicular to the densification direction. In addition, specimens of the shorter configuration were machined parallel to the pressing direction. This was done to investigate any potential strength anisotropy introduced by the PAD operation. The number of specimens machined of each configuration can be found in table 1. Drawings of the tensile specimens can be found in appendix A.

Table 1. Specifications for the tensile specimens.

Block	Length (mm)	Parallel/ Perpendicular	Gauge Section Volume (mm³)	Gauge Section Area (mm²)	Number of Specimens
1	100	Parallel	475	346	10
1	100	Perpendicular	475	346	10
2	100	Parallel	475	346	10
2	100	Perpendicular	475	346	10
1	160	Parallel	1100	696	20

Larger specimens were loaded in uniaxial tension at a loading rate of 93 kN/min using an Instron* 55R1127 load frame.† Smaller specimens were loaded at 71.3 kN/min. These loading rates allowed for a consistent stress rate ($\dot{\sigma}$) of 50 MPa/sec. Specimens were loaded using a self-aligning fixture, shown in figure 4. Annealed copper collets were used to grip and evenly apply load to the end of the specimens.

Figure 4. Uniaxial tensile strength testing configuration showing: (a) specimen fixture with coolant ports, (b) SolidWorks* cutaway view of specimen fixture showing copper collet gripping mechanism.

The microstructure of all specimen types was studied by mounting and polishing the button head ends of failed tensile specimens. SEM was used to take micrographs for grain size measurement. The linear intercept method was used to characterize the grain size.

After tensile testing, optical fractography of the fracture surfaces was used to determine the location, and if possible, identity of the fracture origin of all of the tested specimens. Selected specimens were examined using SEM and Energy Dispersive Spectroscopy (EDS) to further interrogate the structure and composition of specific flaw types. Once flaw types were determined, Weibull statistics were used to describe the strength distributions. Strength-size scaling using the two specimen geometries was attempted. ASTM standard testing methods were used wherever applicable during testing and analysis. Standard test methods used were: ASTM C1239 (Weibull Analysis), ASTM C1683 (Strength-Size Scaling), ASTM C1273 (Tensile Strength), and ASTM C1322 (Fractography) (*16, 20, 24, 25*).

---

* SolidWorks is a registered trademark of Dassault Systèmes SolidWorks Corporation.

3. Results and Discussion

3.1 Microstructure

Using the linear intercept method, the average grain size was measured to be 3 μm. SiC grains from all blocks and specimen orientations were equiaxed with no discernible preferred orientation. In addition to SiC grains, all specimens displayed varying amounts of a second phase. Figure 5 shows both the SiC grain structure (dark) as well as the second phase (light) of a typical microstructure. The second phase was noticed in every micrograph, regardless of specimen orientation; however, there was a large variance in the amount of second phase observed from specimen to specimen. This indicates that the distribution of the second phase was not uniform, potentially affecting the strength of each specimen differently depending upon where they were located in the parent block. A specimen's original location within the parent block was not recorded during specimen machining, thus it may be that the uneven distribution of the second phase may have impacted sample sets to different degrees.

Energy Dispersive Spectroscopy (EDS) was used to determine the elemental makeup of the second phase. The spectrum, seen in figure 6, was devoid of either silicon (Si) or carbon (C), and rich in both aluminum (Al) and oxygen (O). The microstructures in figure 5 suggest a venous intergranular morphology. The presence of an alumina rich second phase was not anticipated and is therefore considered a contaminant.

The most likely source of the alumina contamination is from the grinding media used during ball milling the powder. Alumina grinding media is commonly used in the processing of SiC powders, and it is reasonable that some alumina could enter the ground powder. The amount of alumina observed in figure 5 indicates a large level of contamination, possibly from substantially degraded grinding media.
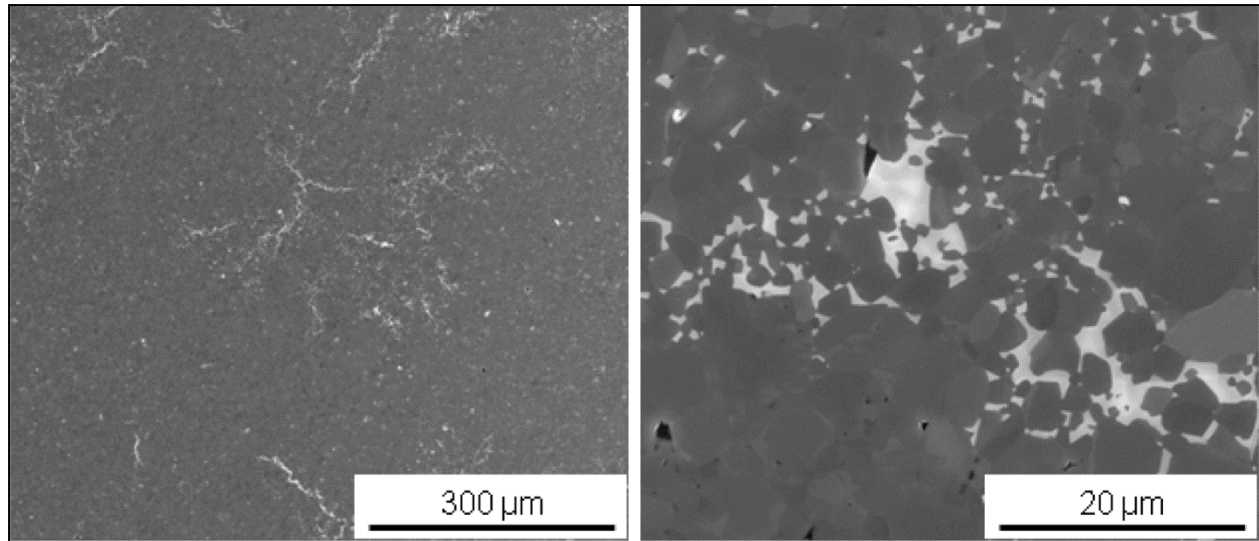
Figure 5. Microstructure showing concentrations of alumina-rich secondary phase in a field of equiaxed SiC grains.
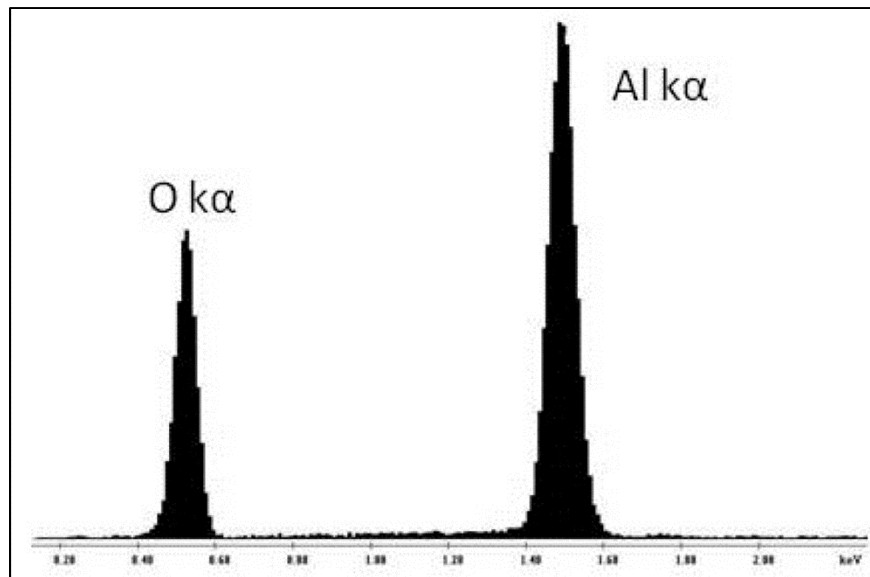
Figure 6. EDS spectra of secondary phase in a SiC specimen showing oxygen and aluminum peaks.

3.2 Strength Results

The average strength values from the uniaxial tension tests can be seen in figure 7. The results are grouped by specimen size and orientation, and include all test results regardless of the fracture origin. Individual specimen information regarding geometry, fracture strength, and flaw type is available in appendix B. The plotted average strength varies widely between samples (even when holding orientation to the densification direction constant), with universally wide standard deviations. The wide standard deviation and lack of a clear trend in the average strength data make drawing conclusions difficult. One possible reason for the wide variance in strengths

9

is the existence of the contaminating alumina phase, seen in figure 5. If this contaminant acts as a strength limiting flaw, it could add a substantial amount of variability to the uniaxial tensile data, given the uneven distribution of the phase observed. The possibility of other strength limiting flaws in addition to the contaminating alumina necessitates thorough fractography. The fractography results are combined with Weibull statistics to shed further light on the strength data.

Tensile specimens with two different effective volumes (475 and 1100 mm^3) were tested in order to determine the effect of strength-size scaling on SiC. The average strengths of these two specimen sizes, when all strength data from both blocks orientations are combined, were 226 and 267 MPa, respectively. Strength-size scaling predicts a lower strength for specimens with a larger effective volume; however, the large variability seen in the strength measurements likely obscures this effect. A more detailed strength-size scaling analysis is presented in section 4.5.
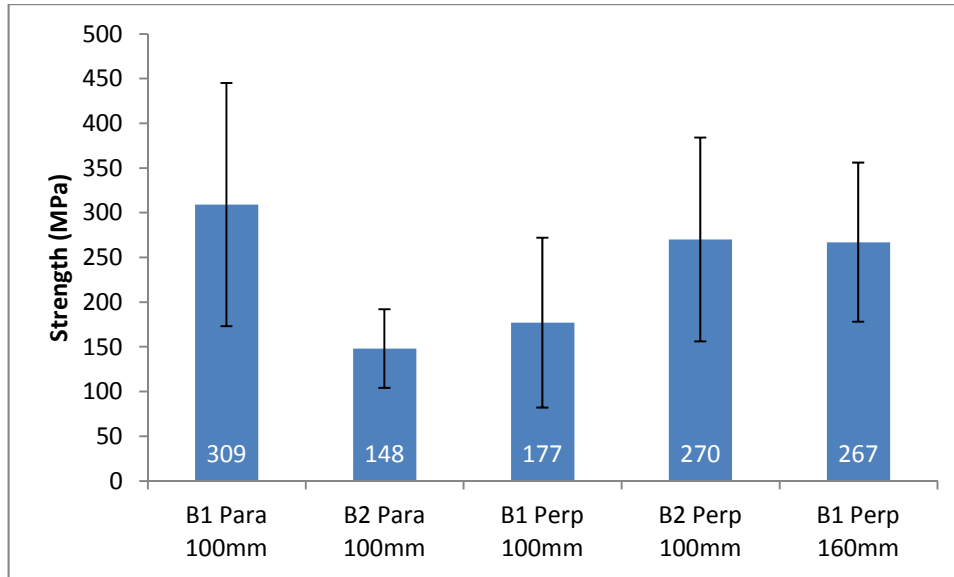
Figure 7. Average tensile strength of all samples.

3.3   Fractography

Optical fractography with a WILD stereo-optical microscope was conducted on all tested specimens. SEM analysis was conducted on selected specimens. Common flaws from which fracture occurred were machining damage (20%), agglomerates (8%), and inclusions (67%). No fracture origin was identified for a small portion (5%) of tensile specimens. Examples of machining damage, agglomerates, and inclusions can be seen in figures 8 and 11. Figure 12 is a fractography montage showing examples of all flaw types as a function of strength and specimen type. Agglomerates appear to have the greatest impact on strength as specimens that had this origin had some of the lowest strength values. Specimens fracturing from inclusions or machining damage have a large range of strength values.

10

Mitigation of machining/handling damage is one of the chief concerns when testing ceramic or other brittle materials. Grinding is done in stages with progressively finer grit sizes to allow the removal of grinding damage introduced during rough machining (*13*). The depth of grinding damage does not correlate with a materials surface finish, meaning that the final specimen surface can hide the existence of severe grinding cracks. Abrasive grinding or cutting creates damage parallel to the grinding direction that can often penetrate much farther (10–20 times) into the ceramic than the observed surface finish indicates. Cracks perpendicular to the grinding direction also occur, but these are usually less severe than those created parallel to the grinding direction. It is for this reason that ceramic tensile specimens are ground longitudinally, orienting the less severe grinding damage perpendicular to the primary tensile axis. Machining damage was the cause of 20% of the fractures studied, and was present in all sample configurations. The presence of machining damage did not necessarily result in a low strength value, even in cases where the machining damage was evident on the tensile surface with the naked eye prior to testing. An example of machining damage can be seen in figure 8. In this example, machining cracks extending beneath the outer surface of the specimen combined to form the strength limiting flaw. It is often the case for many machining flaws to link up to form the strength limiting flaw; therefore, it is helpful to use equation 1 to help validate a measured flaw size. In the case of machining damage, the value of Y can be determined using the Newman-Raju equations (*13*). Using a flaw size of (a = 56 μm, 2c = 220 μm), the Newman-Raju equations predict a Y value of 1.58. Using these parameters, equation 1 predicts a strength of 380 MPa, a value far from the measured strength of 115 MPa. A surface flaw with a strength of 115 MPa would be expected to have a depth of approximately 600 μm. Figure 8 (inset) clearly shows a surface flaw far smaller than 600 μm, with clear machining damage shown in the SEM micrograph. The discrepancy between the measured strength and predicted strength could be due to several factors including slow crack growth, locally reduced fracture toughness, or a local internal stress gradient (*15*).
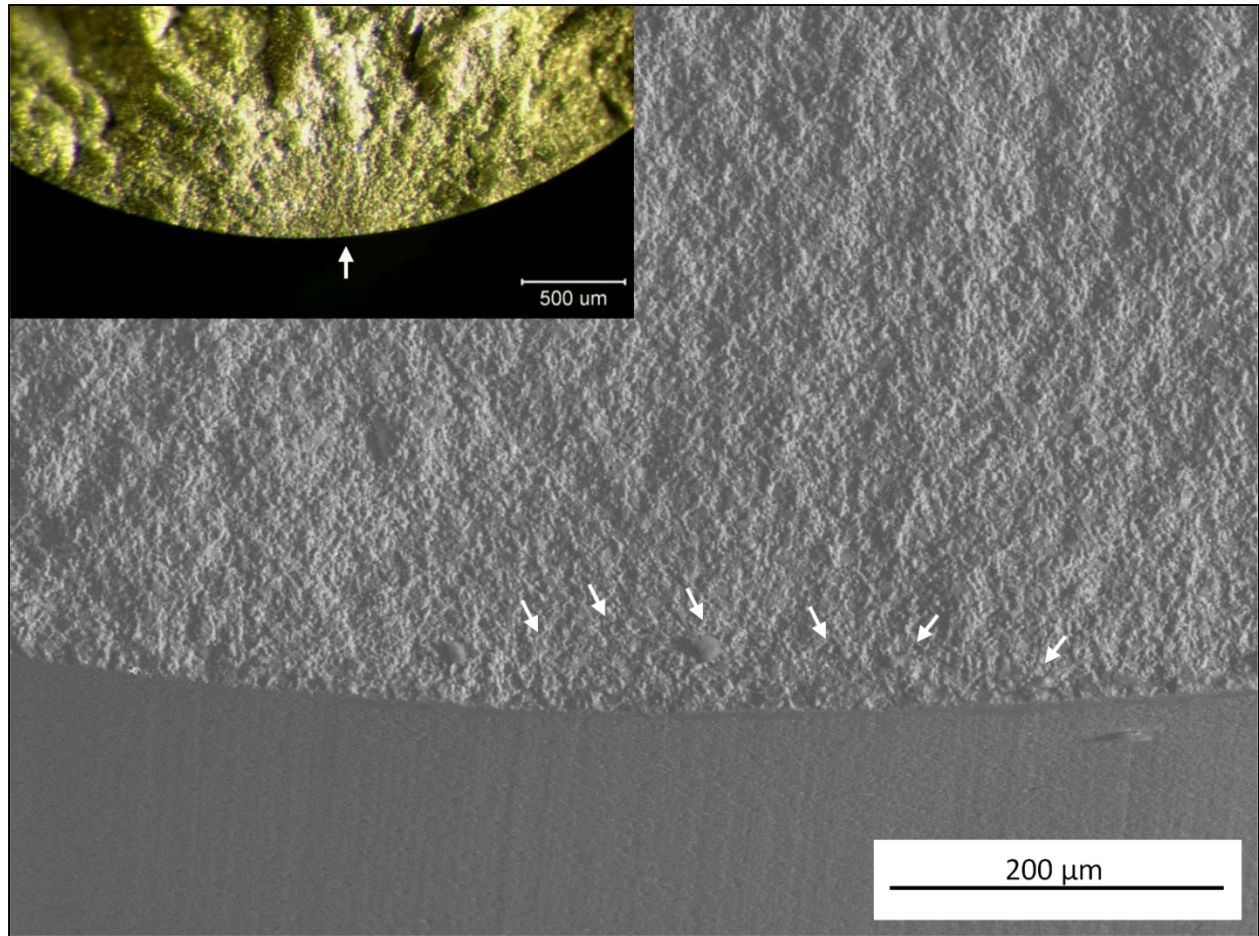
Figure 8. Optical and SEM micrographs of a tensile specimen showing failure from machining damage, indicated by arrows. Tensile strength was 115 MPa.

Agglomerate, as defined in ASTM 1322, is "a volume-distributed flaw that is a cluster of grains, particles, platelets, or whiskers, or a combination thereof, present in a larger solid mass." Agglomerates, seen in figure 9, were composed of clusters of smaller grains within the bulk microstructure. Agglomerates were observed to be of triangular or elliptical geometry, with major axis diameters ranging from approximately 130–300 μm in cross section. The specimen shown in figure 9 demonstrated a tensile strength of 67 MPa. Equation 1 ($K_{IC} = 4.5 \text{MPa}\sqrt{m}$, Y = 1.47) predicts a flaw size of approximately 4175 μm, obviously larger than the observed flaw size. This could indicate the presence of internal stress, low local fracture toughness, or some other factor leading to an overestimation of flaw size (*15*). An estimated flaw size of 300 μm can be obtained by assuming a lowered fracture toughness ($K_{IC} = 3 \text{MPa}\sqrt{m}$) and a 167 MPa stress at the flaw location. The measured fracture strength for this flaw was 67 MPa indicating that, in this scenario, a local internal stress on the order of 100 MPa could be present. This analysis does not confirm the existence of an internal stress of this magnitude; however, local internal stress is a possible reason for the discrepancy between the predicted and observed flaw size. Figure 12 indicates that specimens with this flaw type tend to have some of the lowest

12

strength values. Fracture from agglomerates was exclusively related to specimens machined from the first large SiC block tested. This could point to differences in the preparation of the two blocks; however, specific details on fabrication were not available.
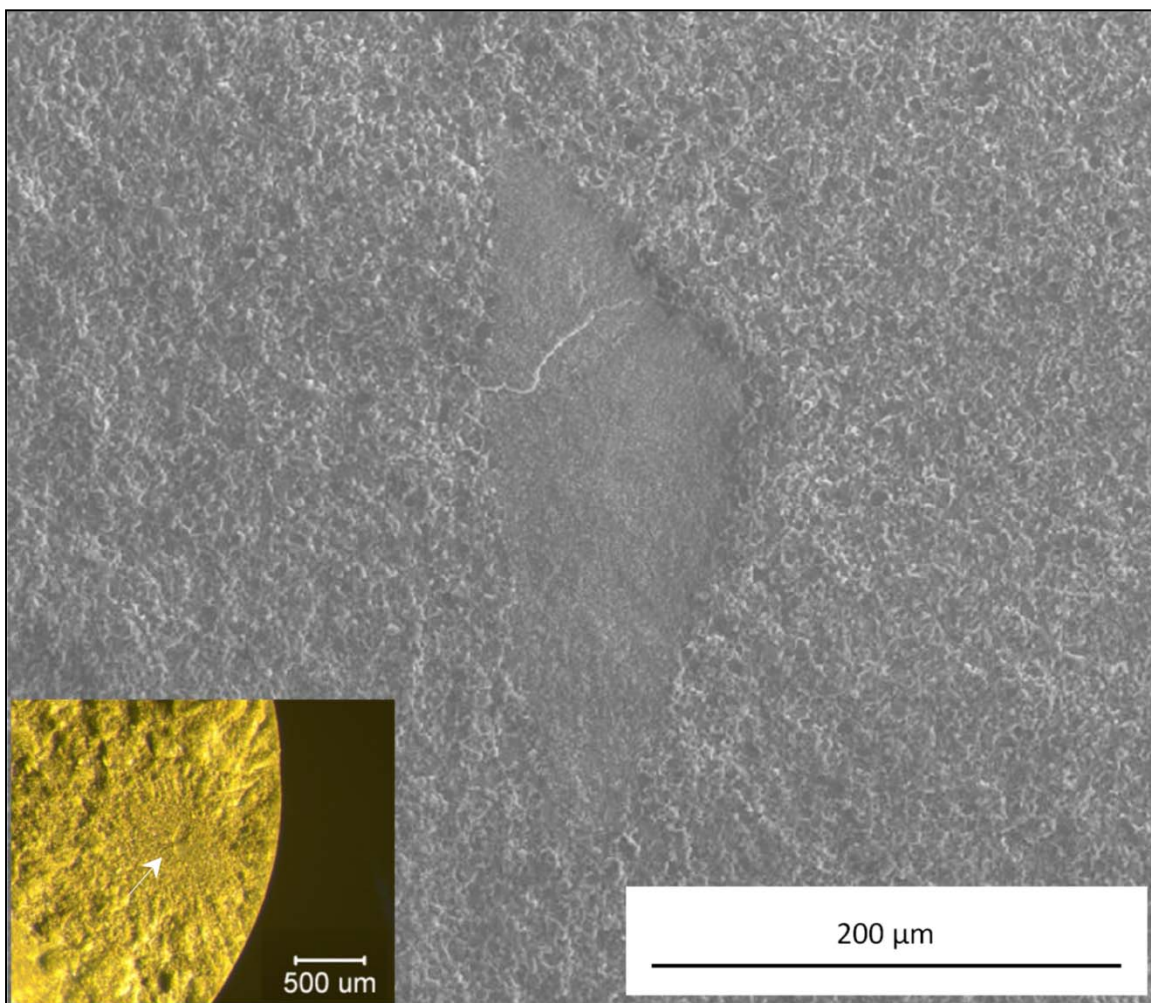
Figure 9. Fracture surface of a specimen that failed from an agglomerate at 67 MPa.

Inclusion, as defined in ASTM 1322, is "a volume-distributed flaw that is a foreign body that has a composition different from the nominal composition of the bulk ceramic." Two different compositions of inclusions were observed. The first, and most prominent, inclusion is related to the Al/O phase seen previously in figure 5. SEM images of these inclusions acting as a fracture origin can be seen in figure 10, and are confirmed chemically using EDS. Inclusions of this type resulted in a broad range of tensile strengths, which correlate with the varying sizes and orientations of the Al/O veins seen in the microstructure. This type of inclusion typically exhibited a long, thin, intergranular morphology. Flaws of this type were observed to be between 100–600 µm in length, with a length/width aspect ratio of greater than 10:1. Using these observed flaw sizes in equation 1 (K_{IC} = 4.5 MPa√m, Y = 1.77), predicted strengths range from 146–359 MPa. The observed strength of the specimen shown in figure 10a was 480 MPa, with an

observed alumina inclusion approximately 100 μm in length. This could indicate that a portion of the alumina inclusion functioned as the critical flaw, with the rest of the flaw exposed by the propagating crack.
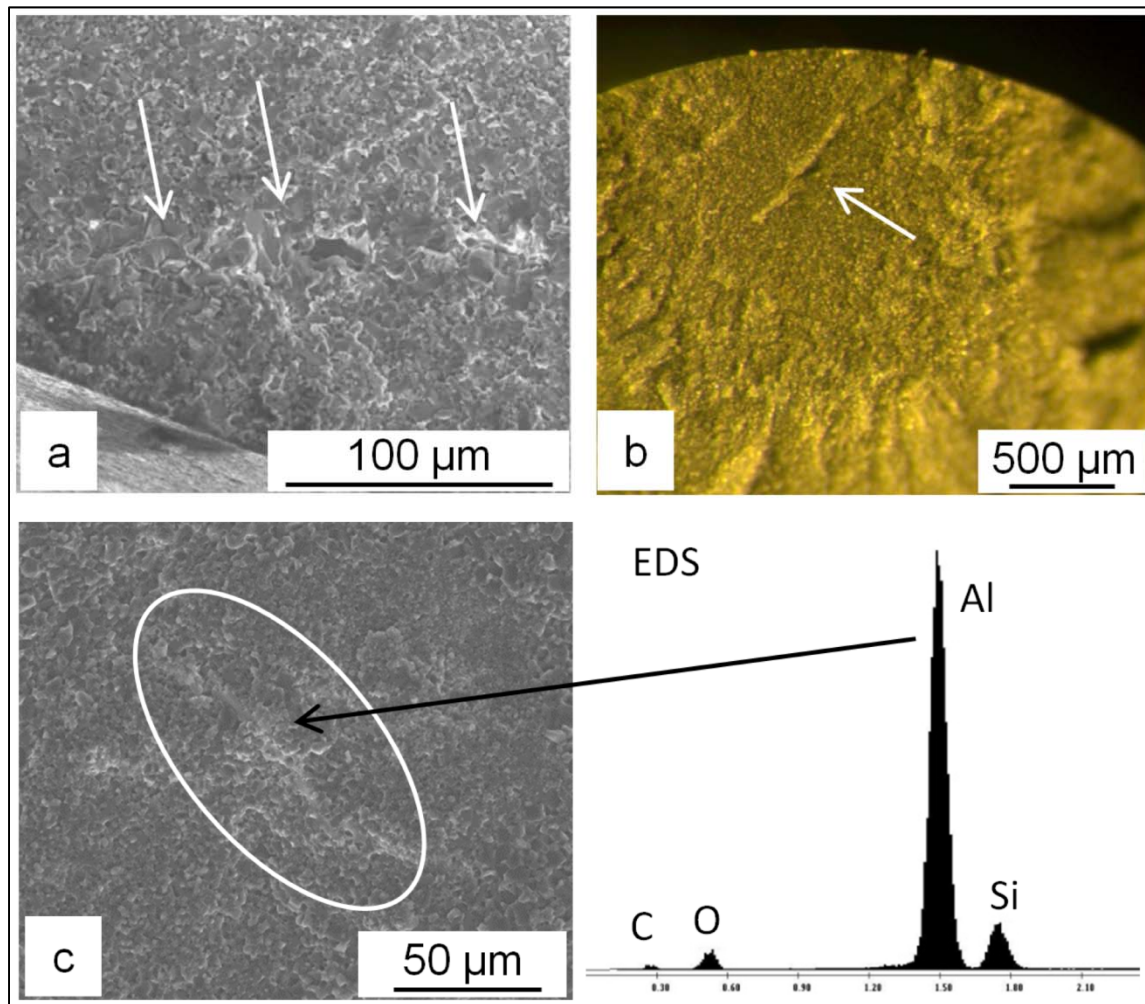
Figure 10. Fracture origins of specimens failing from an alumina rich inclusion. Specimen strengths for images a–c are 480 MPa, 276 MPa, and 151 MPa, respectively.

The second type of inclusion was less common and can be seen in figure 11. A backscatter electron SEM micrograph shows a rectangular flaw with side lengths of 60 and 145 μm, respectively. EDS spectra (not shown) of this inclusion showed high concentrations of Fe, Ni, and Cr. Equation 1 (K_{IC} = 4.5 MPa√m, Y = 1.47) predicts a flaw size of 151 μm, in good agreement with the measured flaw size.

Inclusions, by their definition, are contaminates foreign to the normal composition of a material. Thus, there should be a discrete source of a given inclusion. This knowledge then can be used in a production environment to direct quality improvement efforts to remove sources of contamination. In the case of the Al/O rich inclusion, a possible source of this contamination is

14

the breakdown of Al_2O_3 grinding media during the ball milling stage of powder processing. This is feasible given that alumina is commonly used for this purpose. The second inclusion with a composition rich in Fe, Ni, and Cr resembles the composition of a stainless steel. This could be introduced through any of a number of sources including raw material storage containers, milling containers, sieves, or other powder processing equipment.

Figure 11. Optical and backscatter electron image of the fracture origin (inclusion) of a tensile specimen with a strength of 352 MPa.

Figure 12. Fracture strength and flaw type sorted by sample.

3.4 Weibull Analysis

The Weibull distribution was first described in 1939 by Waloddi Weibull and is used to describe distributions that rely on the "weakest link" theory (*8*). By assuming that the weakest link in a material is the critical flaw from which fracture occurs, the Weibull distribution can be applied to determine metrics for reliability as well as the probability of fracture at a given loa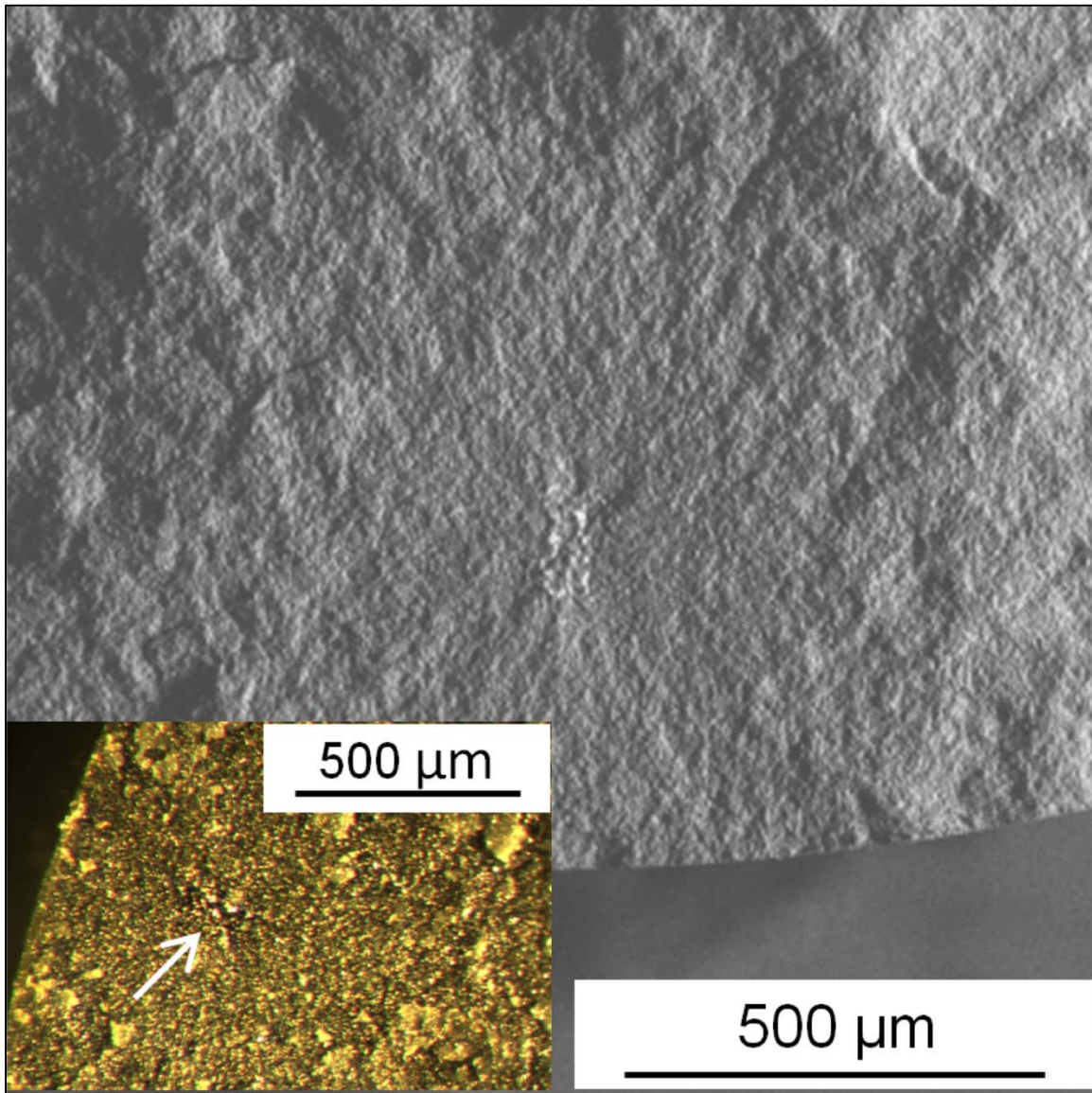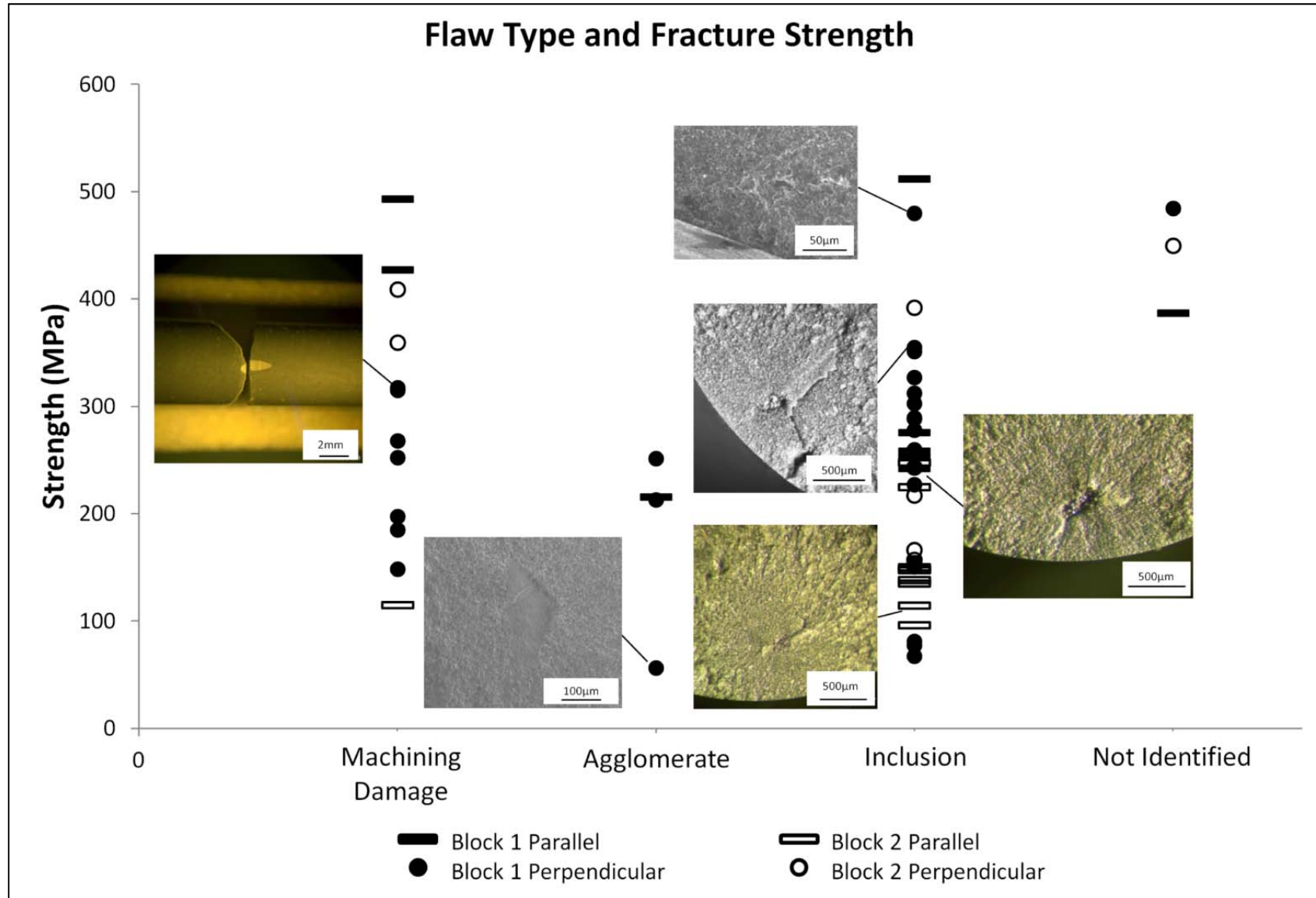d. The Weibull distribution can be seen in equation 2. Where P_f is the probability of fracture, σ is the applied stress at fracture, and m and σ_θ are Weibull constants called the Weibull modulus and the characteristic strength, respectively. Equation 2 may be linearized by taking the double natural log. This is seen in equation 3. The probability of fracture is calculated by ranking the fracture strengths of all specimens from weakest to strongest. The probability of fracture is then calculated for a given specimen using equation 4, where i is the rank order of the specimen strength and n is the total number of specimens. A Weibull plot is constructed by plotting equation 3 as a function of $\ln(\sigma)$, thus giving a straight line with slope equal to the Weibull modulus and x-intercept equal to the characteristic strength. The x-intercept corresponds to $P_f = 0.632$ or a failure probability of 63.2% (*10, 16, 26*). Equation 2 is the two-parameter Weibull distribution. Equation 3 is the linearized two-parameter Weibull distribution. Equation 4 is the probability of failure for the Weibull distribution.

$$P_f = 1 - e^{-\left(\frac{\sigma}{\sigma_\theta}\right)^m} \qquad (2)$$

$$\ln\ln\left(\frac{1}{1-P_f}\right) = m\ln(\sigma) - m\ln(\sigma_\theta) \qquad (3)$$

$$P_f = \left(\frac{i-0.5}{n}\right) \qquad (4)$$

The above analysis is relevant for a sample set of a given loading configuration, flaw population, and effective area (or volume). Each of these factors can change the behavior of one or both of the Weibull parameters. Methods of combining samples of different sizes and different flaw populations have been developed. These have been introduced by Johnson (*11*). The software package WeibPar* (v4.3.0.252) has been developed to assist in combining samples with varying specimen sizes, flaw populations, and testing methods and was used by the authors in this analysis. All WeibPar analyses were done using a Maximum Likelihood Estimation (MLE) regression algorithm. Weibull statistics are affected by the number of specimens used in the calculation of the probability of failure. It is obvious from equation 4 that a sample size with too few specimens will offer very poor failure probability resolution. ASTM C1239 recommends a sample size of 30 specimens for a well defined set of Weibull parameters.

The strength data from figure 12 will be presented with Weibull statistics several different ways. Weibull graphs of the individual data series can be seen in figure 13. Plotted individually, these Weibull distributions show that there is a variation in the Weibull modulus and characteristic

---

strength of the individual series. The plot with the highest Weibull modulus (and lowest characteristic strength) was "B2 Para 100 mm." All of these specimens fractured from either inclusions or machining damage. The series with the highest characteristic strength was "B1 Para 100 mm" with specimens fracturing from at least one of every flaw type. It is interesting that these two data series were from the same testing condition and specimen geometry, only differing in the large SiC block from which they were cut. This speaks to the variability experienced in these large blocks. This variability makes it very difficult to use strength-size scaling to predict the strength.
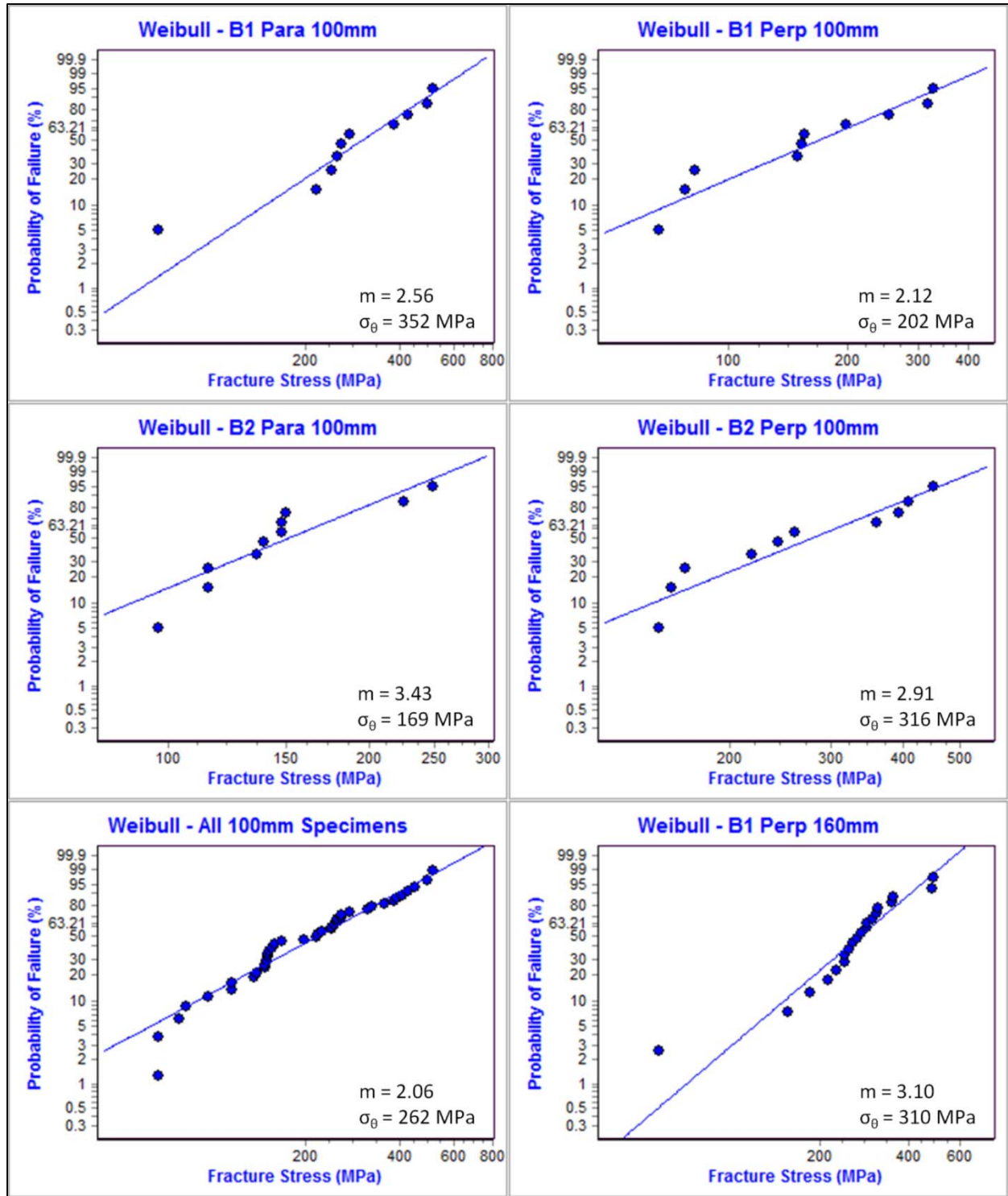
Figure 13. Weibull plots of individual sample series.

For the purpose of Weibull analysis, the strength data taken from the 100-mm specimens can either be considered as four separate groups due to their unique characteristics or as one dataset because of the constant effective volume. This grouping allows for a more refined calculation of

the Weibull parameters. The results of both analyses are displayed in table 2. The Weibull moduli and characteristic strengths of all specimens are uniformly low when compared to the data presented on SiC-N by either Ray et al. or Wereszczak et al., even considering the differences in test methodology (*21, 22*). A likely reason for the low Weibull modulus is the varied flaw populations observed through fractography as well as apparent variability in the material across and between the large blocks. A sample series containing several flaw populations with a wide distribution in sizes will tend to have a lower Weibull modulus than a sample series with a population of relatively consistent flaws. It is common when reporting Weibull parameters to include either the 90% or 95% confidence bounds to indicate the statistical uncertainty associated with the Weibull analysis. The procedure for calculating the confidence bounds associated with populations with multiple concurrent flaw populations are not well developed in Weibpar, thus these values are not reported in table 2.

Table 2. Tabulated Weibull moduli and
characteristic strengths.

Series (mm)	(m)	σ_θ (MPa)
B1 Para 100	2.56	352
B2 Para 100	3.43	169
B1 Perp 100	2.12	202
B2 Perp 100	2.91	316
100 Combined	2.06	262
B1 Perp 160	3.10	310

3.5 Strength-Size Scaling

In the present experiments, two different specimen sizes were studied with the goal of being able to characterize the effect of specimen size on the strength of SiC-N. The two specimen sizes and associated effective surface (S_E) and effective volume (V_E) are found in table 1. The effect of effective surface area (or volume) on the strength of a material can be seen by plotting the log of the strength (mean or characteristic) of a material versus the log of the specimen effective surface area (or volume) over several different specimen sizes. The slope of this line yields the negative inverse of the Weibull modulus. Area or volume is chosen based on the flaw population under consideration. Machining damage should be studied using effective surface area, while volume distributed flaws should be studied using effective volume. Direct calculations given a specific Weibull modulus (m) can be made via equation 5, taken from ASTM C1683 (*20*). Effective volume (V_E) in this equation can be replaced by the effective surface area (S_E). The characteristic strength (σ_θ) can be substituted with the average strength. Equation 5 demonstrates the strength-size scaling relationship.

$$\frac{(\sigma_{\theta,1})}{(\sigma_{\theta,2})} = \left[\frac{V_{E,2}}{V_{E,1}}\right]^{1/m} \tag{5}$$

Strength-size scaling as presented in ASTM C1683 is enabled by seven important assumptions taken from section 5.5 of the ASTM standard.

It is assumed that the same specific flaw type controls strength in the various specimen configurations.

- The material is uniform, homogeneous, and isotropic.

- The material fractures in a brittle fashion.

- The material is consistent (batch-to-batch, day-to-day, etc.).

- The strength distribution follows a two-parameter Weibull distribution.

- Each test piece has a statistically significant number of flaws and they are randomly distributed.

- Flaws are small relative to the specimen cross section size.

It is also noted that if multiple flaw types are present and control strength, then strengths may scale differently for each flaw type (*20*).

Given that there have been four distinct strength controlling flaw types identified in this material through fractography; the first assumption is not met. Furthermore, the distribution of the alumina phase in the SiC was observed to be distributed unevenly throughout the bulk. This brings into question the second assumption. Material inconsistency is also an issue. If flaws such as the agglomerates and inclusions identified previously were uncommon in a normal production environment, the data generated in this study would be of limited use. It is reasonable to state that the other strength-size scaling assumptions have been met. The fact that three of the seven stated assumptions cannot be met calls any strength-size scaling done with this material into serious question and validates the concerns about the value of strength-size scaling in this instance. Figure 14 shows the deviation between strength-size scaling and the observed results. Here, the characteristic strength is scaled using the 160-mm specimen size and Weibull modulus. There is a significant difference between the predicted and actual strength values.

21
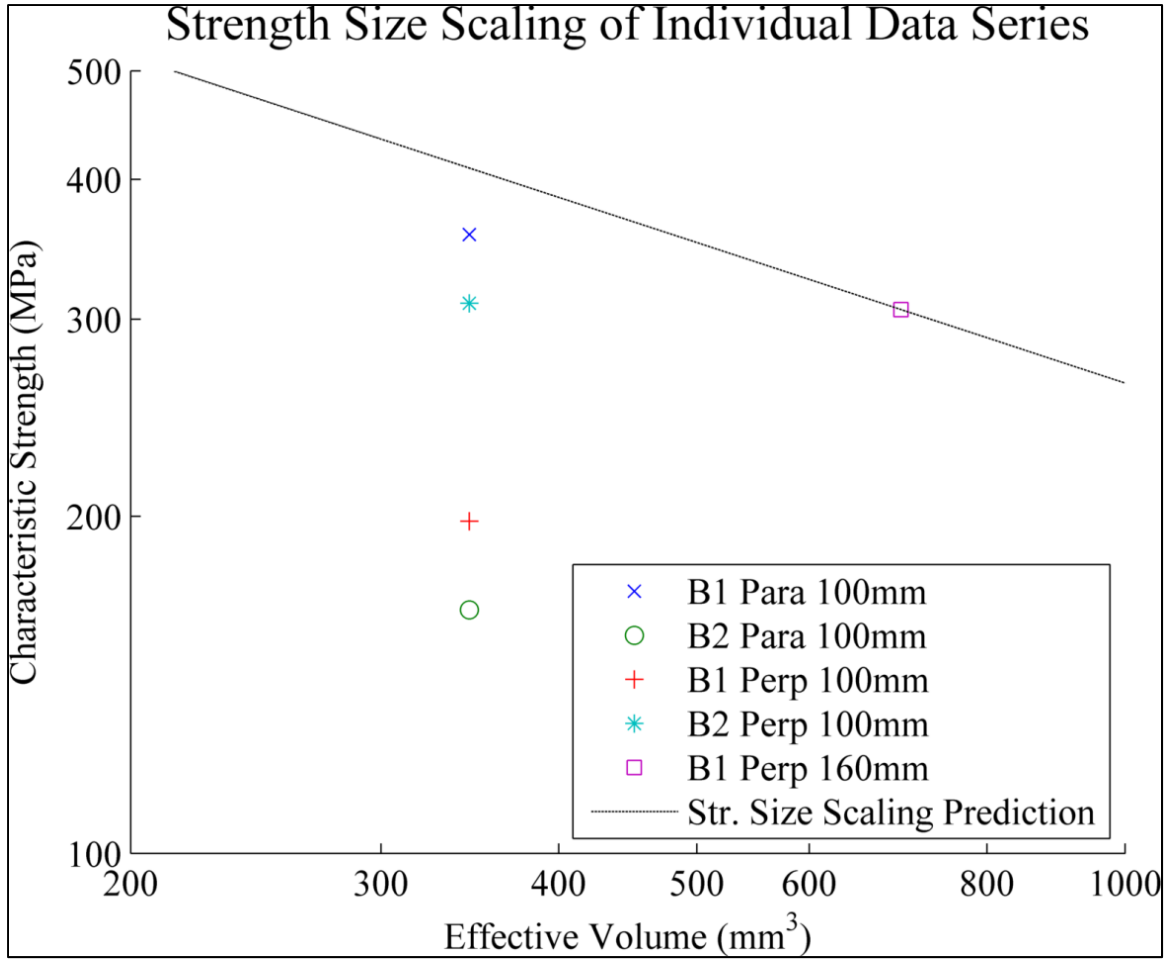
Figure 14. Strength-size scaling prediction of the 160-mm specimen series as a function of effective volume.

One way to improve the size-scaling analysis would be to only consider specimens that fractured from a single flaw type. This would require enough specimens to establish a reliable Weibull modulus and characteristic strength. There are not enough specimens fracturing from a single flaw type to compare between sample series, but machining damage from the 100-mm specimens could be compared to previously published data as a function of effective area because previously published data fractured predominately from machining damage (*22*). In the present data, there were 10 flaws fracturing from machining damage between all sample series with a Weibull modulus of ($m = 2.46$) and characteristic strength of ($\sigma_\theta = 321$ MPa).

Figure 15 shows the scaling of 10 specimens that fractured due to machining damage in this report to data from Ray et al. and Wereszczak et al. (*21, 22*). Even when only considering machining damage, the samples manufactured from the large SiC-N monoliths do not compare favorably with previously published data. In addition to a low characteristic strength exhibited by the present samples, the Weibull modulus does not support strength-size scaling. In figure 15, the modulus of ($m = 2.45$) corresponds to that of the specimens in this study. The modulus of

22

(m = 6.6) is the value reported by Wereszczak et al. (*22*). The data from Wereszczak et al. scales with the Weibull modulus of (m = 6.6) and agrees with the data reported by Ray et al (*21*). The material tested in this report does not scale well with either of the previous data sets. Even if the characteristic strength of the present data was similar to historical data, strength-size scaling would not be advisable because of the low Weibull modulus. The inconsistencies shown in the studied material—both within a single SiC-N block and between the two blocks combined with the low characteristic strength and Weibull modulus—raise concerns about the quality and consistency of this material when fabricated in such large pieces.

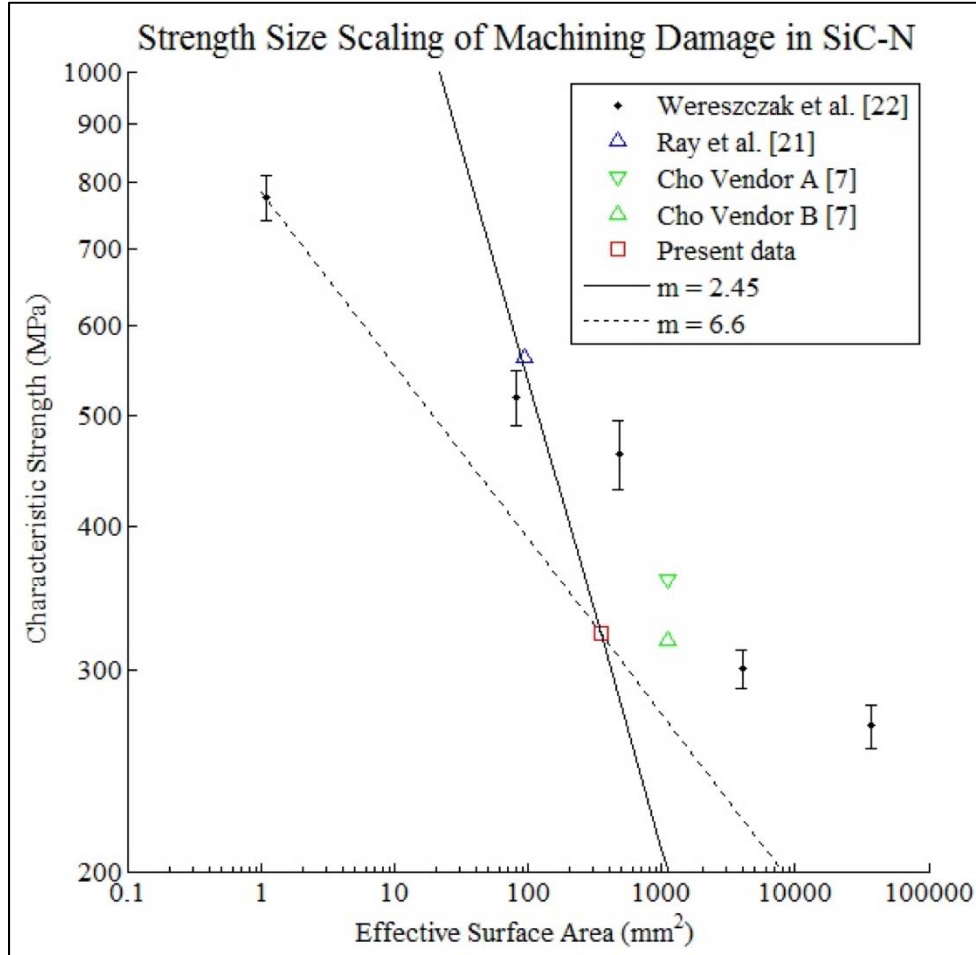Figure 15. Strength-size scaling of present data to previously published results.

4. New Specimen Design

The specimens tested in the current study placed an effective volume of 1100 mm^3 and 475 mm^3 in direct uniaxial tension for the 160- and 100-mm long specimens, respectively. The capability of testing a third effective volume in tension is being considered by redesigning the 100-mm

23

specimen to allow for a gauge section diameter of 3 mm, with the same 20-mm gauge section length. This enables an effective volume of 141 mm^3 to be placed into direct uniaxial tension. An analysis of the von Mises stress of the new specimen geometry placed under 100-MPa uniaxial tension was carried out using SolidWorks Simulation Xpress.[*] The analysis in figure 16 shows the maximum stress located in the gauge section with a smooth transition to lower stress regions. There is observed a slight stress concentration near the buttonhead where the specimen would be gripped by the copper collets (see figure 4); however, this slight increase in stress is minor and should not lead to fracture within the grips. The addition of the smaller specimen size will enable more accurate strength-size scaling of a tested material in the future, while still allowing specimens to be cut from a common (100 × 100 × 18 mm^3) tile configuration. All three specimen sizes can be tested with the same fixture and methodology, allowing direct comparison of results. The technical drawing of the new specimen configuration has been included in appendix A for reference.

---

[*] The use of SolidWorks Simulation Xpress in this report does not constitute endorsement by ARL.
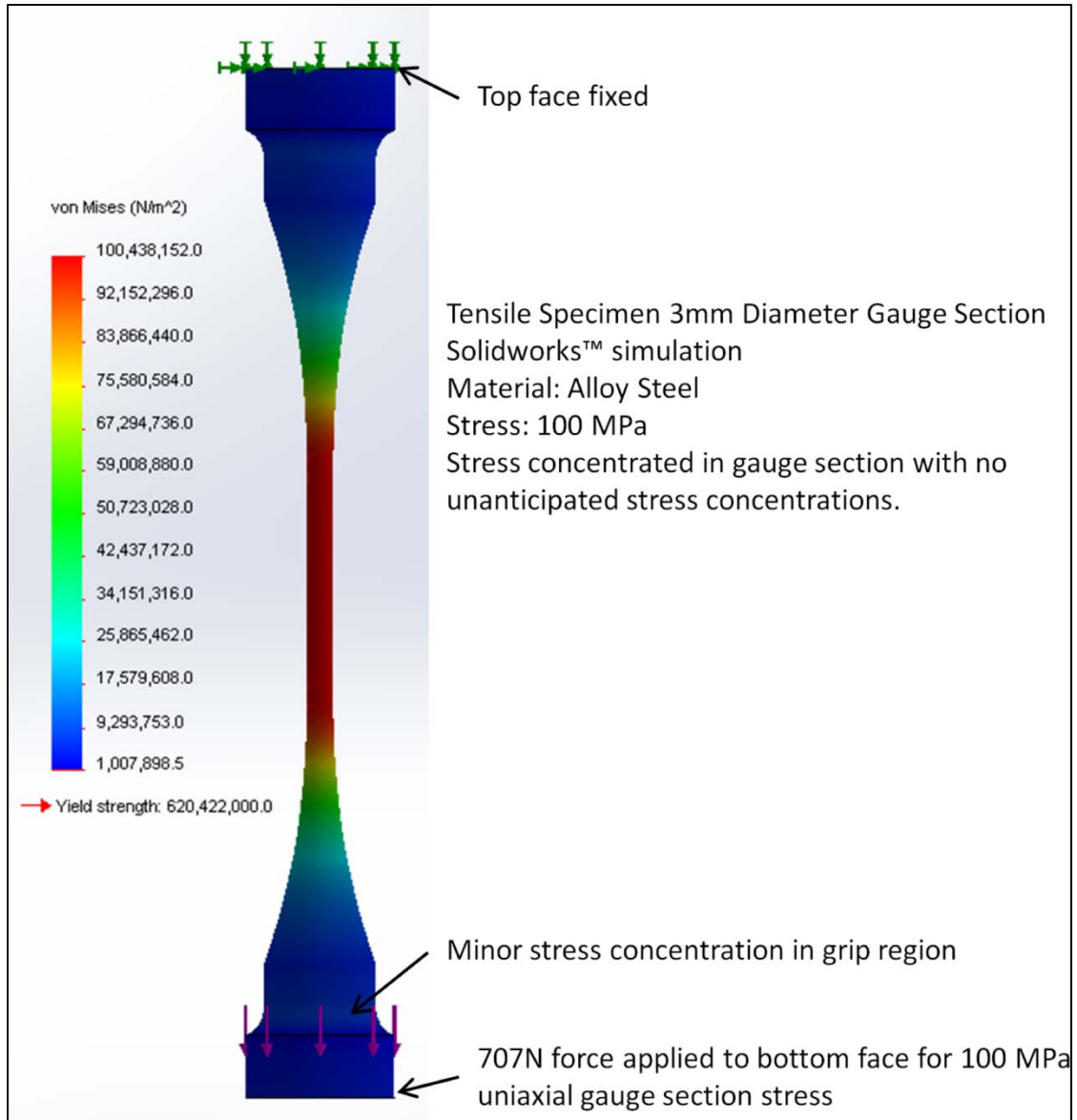
Figure 16. SolidWorks simulation result for 3-mm-diameter gauge-section tensile specimen showing stress concentration in the gauge section.

5. Summary and Conclusions

Large blocks of SiC-N composition were manufactured by BAE Systems (CoorsTek Vista) using pressure aided densification. Uniaxial tensile strength was studied using two different specimen configurations. Specimens were oriented either parallel or perpendicular to the densification direction. Fractographic analysis was accomplished on 100% of tested specimens identifying three critical flaw populations (machining damage, agglomerates, and inclusions). The most

common of these were inclusions that may be due to the degradation and breakdown of Al_2O_3 grinding media during powder processing. Overall, incidents of agglomerates and inclusions were not uniformly distributed between all specimens, leading to a large variance in characteristic strength and low Weibull moduli between each experimental condition.

The wide range of flaw type and severity also prevented traditional strength-size scaling analysis on volume distributed flaws. Comparison of the presented data to historical data sets indicates that the SiC-N material tested was both weaker and less consistent than previously reported, indicating a material of low consistency and poor quality.

Due to the incidence of inclusion related fractures in tested specimens and the low Weibull modulus of this material, it is not recommended that the material properties presented in this report be treated as representative of SiC-N. Furthermore, use of this data for design purposes or the prediction of strength for larger components is strongly discouraged.

6. References

1. Skaggs, S. R. A Brief History of Ceramic Armor Development. In 27th Annual Cocoa Beach Conference on Advanced Ceramics and Composites: A: *Ceramic Engineering and Science Proceedings*, John Wiley & Sons: Inc. New York, NY, 2008, pp. 337–349.

2. Shih, C. J.; Adams, M. A. Ceramic Array Armor, U. P. Office, Editor 2003, Ceradyne, Inc. 6532857, 03/18/2013.3.

3. Anderson, C. E. A Review of Computational Ceramic Armor Modeling. Advances in Ceramic Armor Ii, **2007,** *27* (7), 1–18.

4. Reaugh, J. E.; Holt, A.C.; Wilkins, M.L.; Cunningham, B.J.; Hord, B.L.; Kusubov, A.S. Impact Studies of Five Ceramic Materials and Pyrex. *International Journal of Impact Engineering* **1999**, *23* (1), 771–782.

5. Normandia, M.; LaSalvia, J.C.; Gooch, W.; McCauley, J.W.; Rajendran, A.M. Protecting the Future Force: Ceramics Research Leads to Improved Armor Performance, in AMPTIAC Quarterly2004: New York, NY, p. 21–27.

6. Chen, P.; Kim, G. Y.; Ni, J. Investigations in the Compaction and Sintering of Large Ceramic Parts. *Journal of Materials Processing Technology* **2007**, *190* (1-3) 243–250.

7. Cho, K.; Katz, R. N.; Isa, B. Uniaxial Strength and Mode I Fracture Toughness of Hot Pressed Silicon Carbide (SiC) Materials, U.S. Army Research Laboratory, 1997.

8. Weibull, W. A Statistical Distribution Function of Wide Applicability. *Journal of Applied Mechanics* **1951**, 293–297.

9. Uematsu, K. Immersion Microscopy for Detailed Characterization of Defects in Ceramic Powders and Green Bodies. *Powder Technology* **1996**, *88* (3) 291–298.

10. Jakus, K.; Ritter, J.E.; Service, T.; Sonderman, D. Evaluation of Bimodal Concurrent Flaw Distributions. *Journal of the American Ceramic Society*, **1981**, *64*, (12), C174–C175.

11. Johnson, C. Advanced Statistical Concepts of Fracture in Brittle Materials. *Ceram. Technol. Newsl*. **1988**, *21* (3–5).

12. Li, K.; Warren Liao, T. Surface/Subsurface Damage and the Fracture Strength of Ground Ceramics. *Journal of Materials Processing Technology* **1996**, *57*, (3–4), 207–220.

13. Quinn, G., Practice Guide: Fractography of Ceramics and Glasses National Institute of Standards and Technology, Washington, DC, 2007.

14. Griffith, A. A. Phenomena of Rupture and Flow in Solids. *Philosophical Transactions of the Royal Society of London* **1921**, *21*, 163–198.

15. Quinn, G.; Swab , J. Comparisons of Calculated and Measured Flaw Sizes, in Fourth Alfred Conference on the Fractography of Glasses and Ceramics, J. Varner and G. Quinn, Editors. 2000, The American Ceramic Society: Alfred, NY, p. 175–192.

16. ASTM Standard C1239. Standard Practice for Reporting Uniaxial Strength Data and Estimating Weibull Distribution Parameters for Advanced Ceramics. *International, A,* **2007**, West Conshohocken, PA.

17. ASTM Standard C1161. Standard Test Method for Flexural Strength of Advanced Ceramics at Ambient Temperature. *International, A*, **2008**, West Conshohocken, PA.

18. Quinn, G. D. Weibull Strength Scaling for Standardized Rectangular Flexure Specimens. *Journal of the American Ceramic Society* **2003**, *86* (3), 508–510.

19. Bazant, Z. P. Size Effect on Structural Strength: A Review. *Archive of Applied Mechanics* **1999**, *69* (9–10), 703–725.

20. ASTM Standard C1683. Standard Practice for Size Scaling of Tensile Strengths Using Weibull Statistics for Advanced Ceramics. *International, A*, **2010**, West Conshohocken, PA.

21. Ray, D.; Flinders, R. M.; Anderson, A.; Cutler, R. A.; Campbell, J.; Adams, J. W. Effect of Microstructure and Mechanical Properties on the Ballistic Performance of SiC-Based Ceramics. Advances in Ceramic Armor II. *Ceramic Engineering and Science Proceedings* 2008; Vol. *27*, (7), pp 85–96.

22. Wereszczak, A. A.; Kirkland, T. P.; Strong, K. T.; Campbell, J.; LaSalvia, J. C.; Miller, H. T. Size-Scaling of Tensile Failure Stress in a Hot-Pressed Silicon Carbide. *International Journal of Applied Ceramic Technology* **2010**, *7* (5), 635–642.

23. ASTM Standard C1499. Standard Test Method for Monotonic Equibiaxial Flexural Strength of Advanced Ceramics at Ambient Temperature. *International, A,* **2005**, West Conshohocken, PA.

24. International, A., ASTM Standard C1273 – Standard Test Method for Tensile Strength of Monolithic Advanced Ceramics at Ambient Temperatures, 2000: West Conshohocken, PA.

25. International, A., ASTM Standard C1322 – Standard Practice for Fractography and Characterization of Fracture Origins in Advanced Ceramics, 2005b: West Conshohocken, PA.

26. Hauck, T.; Bohm, C.; Muller, W. H. Weibull Statistics for Multiple Flaw Distributions and Its Application in Silicon Fracture Prediction. Thermal, Mechanical and Multi-Physics Simulation and Experiments in Micro-Electronics and Micro-Systems, 2005: p. 242–247.
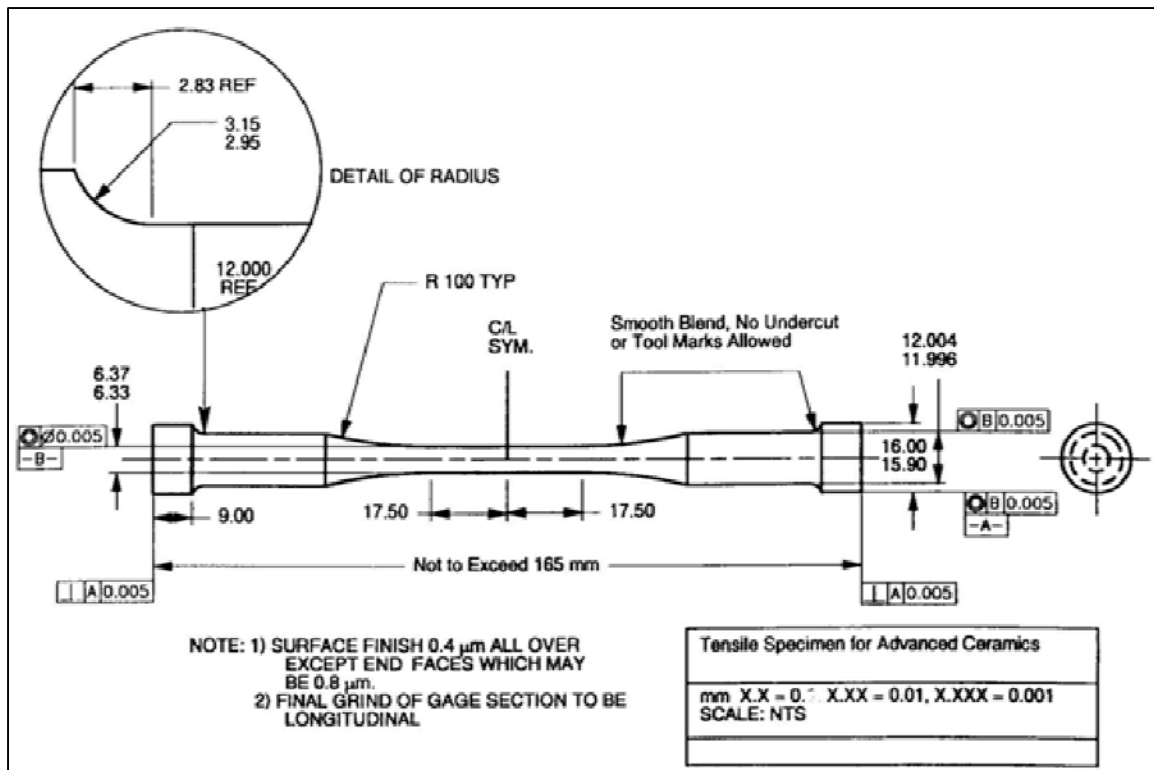
Appendix A. Specimen Part Prints

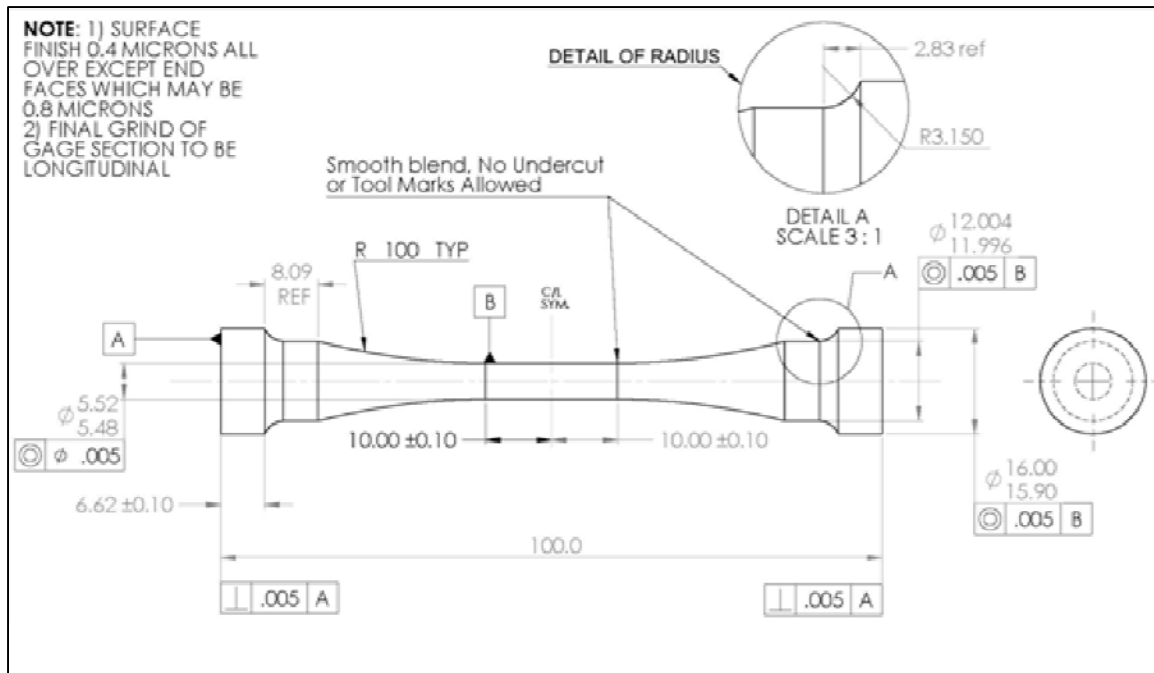Figure A-1. Drawing for 160-mm ceramic-tensile specimen, taken from figure 9 of ASTM C1273.

Figure A-2. Drawing for 100-mm ceramic tensile specimen with 5.5-mm gauge section diameter.

30
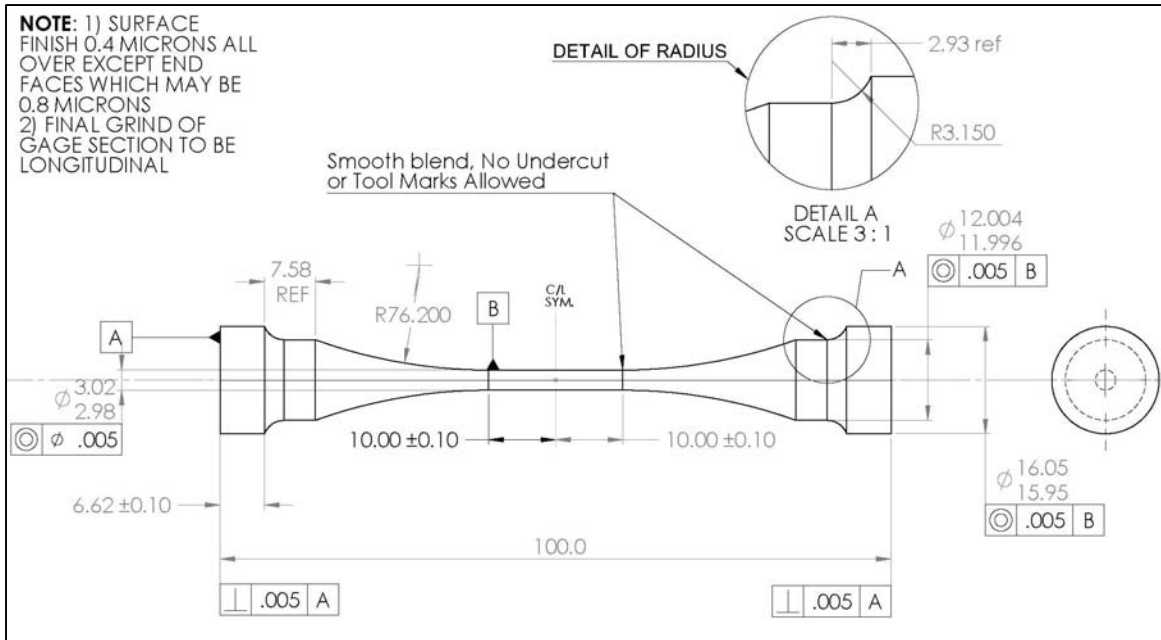
Figure A-3. Drawing for the new ceramic tensile specimen with a 3-mm gauge section diameter.

INTENTIONALLY LEFT BLANK.

Appendix B. Mechanical Properties

Table B-1. Tensile strength data from block 1, 100-mm specimens, parallel to PAD direction.

Block 1 – 100 Parallel					
Tensile Strength Data From Block 1, 100-mm Specimens, Parallel to PAD Direction					
Specimen (No.)	Fracture Load (N)	Gauge Diameter (mm)	Tensile Strength (MPa)	Outside Gauge (Y/N)	Fracture Origin
8	1593	5.51	67	N	Agglomerate
3	5129	5.51	215	N	Agglomerate
5	5769	5.51	242	N	Inclusion
7	6008	5.51	252	N	Inclusion
4	6150	5.54	255	N	Inclusion
1	6560	5.54	272	N	Inclusion
10	9201	5.66	365	Y	Not Identified
9	10158	5.51	426	N	Machining Damage
2	11727	5.54	487	N	Machining Damage
6	12169	5.54	505	N	Inclusion
		Average	309		
		Stdev	124		

Specimen Effective Volume:	475 mm^3	
Stressing Rate:	50 MPa/sec	
Sample Weibull Modulus:	2.56	
Sample Characteristic Strength:	352 MPa	

Table B-2. Tensile strength data from block 1, 100-mm specimens, perpendicular to PAD direction.

Block 1 — 100 Perpendicular					
Tensile Strength Data From Block 1, 100-mm Specimens, Perpendicular to PAD Direction					
Specimen (No.)	Fracture Load (N)	Gauge Diameter (mm)	Tensile Strength (MPa)	Outside Gauge (Y/N)	Fracture Origin
2	1603	5.51	67	N	Inclusion
9	1849	5.54	77	N	Inclusion
3	1938	5.56	80	N	Inclusion
8	3529	5.51	148	N	Machining Damage
6	3645	5.56	150	Y	Inclusion
5	3679	5.51	154	N	Inclusion
1	4701	5.51	197	N	Machining Damage
7	6006	5.51	252	N	Machining Damage
4	7546	5.51	316	N	Machining Damage
10	7778	5.51	326	N	Inclusion
		Average	177		
		Stdev	95		
Specimen Effective Volume:			475 mm^3		
Stressing Rate:			50 MPa/sec		
Sample Weibull Modulus:			2.12		
Sample Characteristic Strength:			202 MPa		

Note: Specimen 6 broke into four pieces, initiation site uncertain.

Table B-3. Tensile strength data from block 2, 100-mm specimens, parallel to PAD direction.

Block 2 – 100 Parallel					
Tensile Strength Data From Block 2, 100-mm Specimens, Parallel to PAD Direction					
Specimen (No.)	Fracture Load (N)	Gauge Diameter (mm)	Tensile Strength (MPa)	Outside Gauge (Y/N)	Fracture Origin
8	2296	5.53	96	N	Inclusion
2	2730	5.59	111	Y	Inclusion
7	2743	5.47	117	N	Machining Damage
6	3221	5.52	135	N	Machining Damage
4	3293	5.44	142	N	Inclusion
10	3507	5.50	148	N	Inclusion
5	3518	5.92	128	Y	Inclusion
3	3575	5.54	148	N	Inclusion
1	5348	5.53	223	N	Inclusion
9	5892	5.73	228	Y	Inclusion
		Average	148		
		Stdev	44		

Specimen Effective Volume:	475 mm^3
Stressing Rate:	50 MPa/sec
Sample Weibull Modulus:	3.43
Sample Characteristic Strength:	169 MPa

Table B-4. Tensile strength data from block 2, 100-mm specimens, perpendicular to PAD direction.

Block 2 – 100 Perpendicular					
Tensile Strength Data From Block 2, 100-mm Specimens, Perpendicular to PAD Direction					
Specimen (No.)	Fracture Load (N)	Gauge Diameter (mm)	Tensile Strength (MPa)	Outside Gauge (Y/N)	Fracture Origin
3	3598	5.60	146	Y	Inclusion
4	3745	5.46	160	N	Inclusion
1	3960	5.49	167	N	Inclusion
6	5170	5.72	201	Y	Inclusion
9	5781	6.09	198	Y	Inclusion
7	6152	5.66	245	Y	Inclusion
2	8554	5.60	347	N	Machining Damage
10	9317	5.58	381	Y	Inclusion
5	9719	5.48	412	N	Machining Damage
8	10689	5.54	443	N	Not Identified
		Average	270		
		Stdev	114		

Specimen Effective Volume:	475 mm^3	
Stressing Rate:	50 MPa/sec	
Sample Weibull Modulus:	2.91	
Sample Characteristic Strength:	316 MPa	

Table B-5. Tensile data from block 1, 160-mm specimens, perpendicular to PAD direction.

Block 1 – 160 Perpendicular					
Tensile Strength Data From Block 1, 160-mm Specimens, Perpendicular to PAD Direction					
Specimen (No.)	Fracture Load (N)	Gauge Diameter (mm)	Tensile Strength (MPa)	Outside Gauge (Y/N)	Fracture Origin
14	1779	6.35	57	N	Agglomerate
12	4875	6.53	136	Y	Inclusion
15	5831	6.40	183	Y	Machining Damage
16	6714	6.53	196	N	Agglomerate
3	7153	6.43	221	N	Inclusion
20	7673	6.32	245	N	Inclusion
9	7680	6.53	213	Y	Inclusion
6	7927	6.38	248	N	Agglomerate
2	8177	6.32	261	N	Inclusion
11	8443	6.30	272	N	Machining Damage
18	8757	6.38	275	N	Inclusion
7	9090	6.38	285	N	Inclusion
5	9117	6.35	288	Y	Inclusion
1	9535	6.30	307	N	Inclusion
13	9839	6.35	313	N	Inclusion
19	9931	6.32	316	N	Machining Damage
4	11068	6.32	353	N	Inclusion
10	11181	6.35	352	N	Inclusion
17	15112	7.11	340	Y	Inclusion
8	15258	6.35	474	N	Not Identified
		Average	267		
		Stdev	89		
Specimen Effective Volume:			1100 mm^3		
Stressing Rate:			50 MPa/sec		
Sample Weibull Modulus:			3.10		
Sample Characteristic Strength:			310 MPa		

Note: Specimen 19 fractured from severe machining damage, visible without magnification. Specimen 4 EDS showed the iron rich inclusion, see figure 11.

List of Symbols, Abbreviations, and Acronyms

Al	aluminum
Al_2O_3	aluminum oxide (alumina)
ARL	U.S. Army Research Laboratory
ASTM	American Society for Testing and Materials
C	carbon
EDS	Energy Dispersive Spectroscopy
m	Weibull modulus
min	minute
MLE	Maximum Likelihood Estimation
O	oxygen
PAD	Pressure Aided Densification
S_E	effective surface area
sec	second
SEM	scanning electron microscopy
Si	silicon
SiC	silicon carbide
V_E	effective volume